Journal of Polymer Science

WILEY

JOURNAL OF
POLYMER SCIENCE

RESEARCH ARTICLE OPEN ACCESS

Ternary Microphase Diagram of SBM Triblock Terpolymer Morphologies in Spherical Confinement

Manuel Trömer[1] | Elias M. Zirdehi[2] | Yorick Post[1] | Arash Nikoubashman[3,4] | André H. Gröschel[1,5]

[1]Institute for Physical Chemistry and Center for Soft Nanoscience (SoN), University of Münster, Münster, Germany | [2]Institute of Physics, Johannes Gutenberg University Mainz, Mainz, Germany | [3]Leibniz-Institut für Polymerforschung Dresden e.V., Dresden, Germany | [4]Institut für Theoretische Physik, Technische Universität Dresden, Dresden, Germany | [5]Bavarian Centre for Battery Technology (BayBatt) and Bavarian Polymer Institute (BPI), University of Bayreuth, Bayreuth, Germany

Correspondence: Arash Nikoubashman (anikouba@ipfdd.de) | André H. Gröschel (andre.groeschel@uni-bayreuth.de)

Received: 23 January 2025 | **Revised:** 12 April 2025 | **Accepted:** 28 April 2025

Funding: This work was supported by Deutsche Forschungsgemeinschaft 445740352, 233630050, 451785257, 470113688.

Keywords: 3D confinement | ABC triblock terpolymers | dissipative particle dynamics | emulsification | microparticles | molecular simulations | ternary phase diagram

ABSTRACT

Block copolymers are a versatile class of soft materials, as they combine different chemical and physical properties within the same macromolecule. Triblock terpolymers are of particular interest because of the numerous morphologies they can form. With the aim of generating a comprehensive ternary microphase diagram, we emulsified 22 different polystyrene-*block*-polybutadiene-*block*-poly(methyl methacrylate) triblock terpolymers and analyzed the morphology of the resulting microparticles after solvent evaporation. We employed controlled confinement conditions using a Shirasu Porous Glass membrane setup and analyzed the microparticles via transmission electron microscopy and tomography, as well as scanning electron microscopy. We identified a wealth of microparticle morphologies, of which several were previously not reported. Experiments were accompanied by coarse-grained molecular simulations, where we correlated the effect of evaporation rate on morphology and particle shape.

1 | Introduction

Block copolymers (BCPs) have become a versatile class of functional soft matter useful for a broad range of applications, including templating of nanostructures [1], filtration membranes [2], the formation of Janus nanoparticles [3], catalysis [4], and nanomedicine [5]. Although traditionally, BCPs were studied for their morphologies in thin films, in bulk [6, 7] or as self-assemblies in solution [8, 9], more recently, their microphase separation within the confinement of emulsion droplets has become of interest. After solvent evaporation, the BCPs form microparticles (MPs) of defined shape and controlled inner order [10–13]. The inner morphology of these MPs imparts them with additional functional properties useful for applications, for example as photonic pigments [14–16], hybrid particles [17, 18] or mesoporous nanostructures [19, 20]. Among the parameters known to influence the morphology of BCP MPs, the chemistry and composition of the blocks are most important, as these predominantly control microphase separation and domain geometry, and thus give rise to different types of morphologies within the MPs (e.g., lamella, cylinder, sphere) [21, 22]. By varying the rate of solvent evaporation [23–25] or the use of block-selective surfactants [26–28], it is possible to change the orientation of the blocks within the MP and thereby control its aspect ratio.

Manuel Trömer and Elias M. Zirdehi contributed equally to this study.

Journal of Polymer Science, 2025; 63:4424–4435
https://doi.org/10.1002/pol.20250090

Although the (directed) assembly of diblock copolymers in confinement is nowadays fairly well understood, there are much fewer experimental [29–39] and theoretical studies [40–43] on the confinement assembly of ABC triblock terpolymers. This knowledge gap is (partly) due to the considerable expansion of possible morphologies offered by the larger number of blocks, as already demonstrated by Stadler on the ternary microphase diagram of polystyrene-*block*-polybutadiene-*block*-poly(methyl methacrylate) (SBM) in bulk [44–46]. The parameter space expands even further for enclosed systems, since one also needs to consider, for example, the shape and wetting properties of the confinement. Our first attempt to transfer the plethora of terpolymer morphologies into confinement, and thus into MPs, only succeeded in part, as the chosen polystyrene-*block*-polybutadiene-*block*-poly(*tert*-butyl methyl methacrylate) (SBT) exhibited peculiar interfacial energies [47] yielding morphologies such as lamella–lamella, axially stacked core–shell rings, and concentric sphere-in-lamella [48].

Here, we combine the chemistry of SBMs with controlled confinement to generate a more comprehensive microphase diagram of ABC triblock terpolymers in spherical MPs. To ensure reproducibility and largely exclude the effect of particle size on morphology, we use the Shirasu Porous Glass (SPG) setup [49] as a means to produce near-monodisperse MPs with diameters of ~600 nm. We systematically vary the block composition of the 22 SBMs and investigate the internal morphologies with scanning and transmission electron microscopy (SEM and TEM), TEM cross-sections, and electron tomography (ET). We complement our experiments with dissipative particle dynamics (DPD) simulations using a coarse-grained SBM model. These results deliver guidelines for the targeted production of several morphologies addressable via controlled confinement.

2 | Experimental Section

2.1 | Materials

Analytical grade solvents and chemicals were used as received unless otherwise noted. Ruthenium chloride ($RuCl_3$, Ru content 45%–55%), iron oxide nanoparticles ($d \approx 20$ nm, 5 g L^{-1} in toluene), and sodium dodecyl sulfate (SDS, $>99\%$) were received from Sigma Aldrich. Osmium tetroxide was obtained from Science Services (OsO_4, 4 wt.% in H_2O). Ultrapure water was provided from a Milli-Q Integral Water Purification System. Regenerated cellulose tubes with a molecular weight cut-off of 12–14 kDa and an average flat width of 33 mm (Sigma Aldrich) were used for dialysis. The polystyrene-*block*-polybutadiene-*block*-poly(methyl methacrylate) triblock terpolymers (PS-*b*-PB-*b*-PMMA or SBM) were synthesized by sequential anionic polymerization as described elsewhere [50]. The SBMs are labeled such that subscripts represent the volume percentages of the respective blocks (which are directly related to their volume fractions Φ), whereas the superscript gives the number average molecular weight (M_n) in kg mol^{-1}, for example $S_{30}B_{42}M_{28}{}^{68}$ (entry 1, Table 1). The values were determined through a combination of size exclusion chromatography (SEC) and nuclear magnetic resonance (NMR).

2.2 | MP Fabrication With SPG Membranes

Each SBM triblock terpolymer was dissolved in chloroform ($CHCl_3$) at a concentration of 10 g L^{-1}. In a typical experiment, 1 mL of polymer solution was emulsified into 20 mL of aqueous surfactant solution containing SDS at a concentration of 5 g L^{-1}. For emulsification, we used pressurized Argon to push the polymer solution into the continuous phase through an SPG membrane with a pore diameter of 600 nm. The emulsion was stirred at 250 rpm and kept stirring for an additional 5 days until $CHCl_3$ had completely evaporated, which resulted in the formation of solid SBM MPs. Excess surfactant was removed by dialysis of the suspension ($c = 0.5$ g L^{-1}) against ultrapure water.

2.3 | TEM Sample Preparation and Measurements

The MPs were typically cross-linked with OsO_4 in solution, which selectively stained the PB microdomain at the same time. For that, 1.2 mL of MP suspension was placed in an open vial, which was then transferred into a closed glass chamber containing another open vial with an OsO_4 solution (4 wt.% in H_2O). The chamber was closed, and the liquids were kept under stirring. After 3 h, the chamber was opened, and the MPs were purified via centrifugation and redispersion in ultrapure water to remove excessive OsO_4. For TEM preparation, a drop of the suspension ($c = 0.5$ g L^{-1}) was placed on a carbon-coated copper grid (400 mesh, Science Services) and excess liquid was blotted after 60 s using a filter paper. For cross-sectioning, the MPs were freeze-dried and then embedded in 3D Rapid Resin CLEAR 3DR3582C, which was cured under UV light ($\lambda = 365$ nm). Sectioning was done on a Reichert/Leica Ultracut E microtome (Leica Microsystems, Wetzlar, Germany), with a velocity of 1 mm s^{-1} at an inclination angle of 6° to generate slices of <100 nm thickness. Cross-sections were then transferred onto copper grids. In addition to staining with OsO_4, where necessary, some samples were stained with RuO_4. For Ru staining, TEM grids containing the sample were placed in a closed glass chamber together with a small amount of $RuCl_3$, which was mixed with 0.5–1 mL of 11%–14% NaOCl solution. The chamber was opened after 15 min of staining. For ET measurements, samples were prepared similarly to the TEM samples, with the exception that beforehand, a drop of iron oxide nanoparticles in toluene ($d \approx 20$ nm, $c = 0.05$ g L^{-1}) was placed on the grid as fiducial markers. Toluene was allowed to evaporate, and the grid was then prepared as described above. Tilt series were recorded in an angular range of $\pm 60°$, where images were taken in 3° steps using Tomography (Thermo Fisher Scientific, Version 5.14.0) to record the tilt series. IMOD (Version 4.11.24) was used to pre-align the tilt series [51] and to calculate the reconstruction. Video S1 can be found in the Supporting Information and was compiled with ImageJ (Version 1.53 k) after alignment. UCSF Chimera (Version 1.17.3) was used to visualize the 3D reconstructions [52].

2.4 | Instruments

TEM measurements were performed on a Talos L120C microscope (Thermo Fisher Scientific) with an acceleration voltage of 120 kV and an $LaBF_6$ filament. Images were taken with a Ceta-F camera and Velox Software (Version 3.8.80). The ImageJ

TABLE 1 | Overview on used SBM triblock terpolymers.

Polymer[a]	M_n[b] (kg mol^{-1})	$Đ$[c]	Inner morphology	MP shape
$S_{30}B_{42}M_{28}$	68	1.02	*ll*	Onion-like
$S_{33}B_{37}M_{30}$	113	1.05	*ll*	Onion-like
$S_{32}B_{40}M_{28}$	125	1.05	*ll*	Onion-like
$S_{32}B_{41}M_{27}$	137	1.09	*ll*	Onion-like/tulip-bulb
$S_{28}B_{40}M_{32}$	144	1.05	*ll*	Onion-like/tulip-bulb
$S_{35}B_{49}M_{16}$	216	1.21	*ll*	Tulip-bulb
$S_{33}B_{45}M_{22}$	231	1.23	*ll*	Prolate ellipsoid
$S_{30}B_{42}M_{28}$	244	1.24	*ll*	Prolate ellipsoid
$S_{34}B_{33}M_{33}$	85	1.13	*lpl*	Onion-like
$S_{40}B_{23}M_{37}$	91	1.06	*lpl*	Onion-like
$S_{41}B_{25}M_{34}$	143	1.09	*lpl*	Prolate ellipsoid
$S_{48}B_{31}M_{24}$	158	1.08	*lpl*	Onion-like
$S_{50}B_{30}M_{20}$	159	1.09	*lpl*	Onion-like
$S_{59}B_{16}M_{25}$	119	1.11	*lr*	Onion-like
$S_{56}B_{16}M_{28}$	125	1.09	*lr*	Onion-like
$S_{55}B_{15}M_{30}$	127	1.09	*lr*	Tulip-bulb
$S_{45}B_{13}M_{42}$	79	1.07	*ls*	Onion-like
$S_{48}B_{11}M_{41}$	80	1.07	*ls*	Onion-like
$S_{46}B_{9}M_{45}$	172	1.08	*ls*	Tulip-bulb/prolate ellipsoid
$S_{78}B_{12}M_{10}$	85	1.05	$s_o s$	Spherical
$S_{74}B_{12}M_{14}$	89	1.06	$c_o c$	Spherical
$S_{33}B_{23}M_{44}$	100	1.10	$c_o c$	Spherical

Abbreviations: $c_o c$ = cylinder-on-cylinder; *ll* = lamella-lamella; *lpl* = lamella-perforated lamella; *lr* = lamella-ring; *ls* = lamella-sphere; $s_o s$ = sphere-on-sphere.

[a] Subscripts indicate the respective volume fraction of the blocks.

[b] Molecular weight (M_n; number average) determined via SEC and ^{1}H-NMR. PS was used as the standard and THF as the eluent.

[c] Dispersity from SEC with PS standards in THF as eluent and a flow rate of 1 mL min^{-1}.

open-source software package (Version 1.53 k) was used for processing the data [53]. Microdomain sizes were measured and averaged over at least 50 different locations. SEM was done on a cryo-field emission microscope (Zeiss Cross Beam 340) equipped with an energy-selective detector for 16-bit image series acquisition with up to 40,000 × 50,000 pixel resolution, and the in-lens chamber was used for SEM imaging. Samples for SEM measurements were prepared by putting one drop of an approximately 0.5 g L^{-1} sample dispersion on a silicon wafer and dried for at least 4 h. The samples were then sputtered with 4 nm Au using a Quorum PP3010T-Cryo chamber with integrated Q150T-Es high-end sputter coater. Dynamic light scattering (DLS) measurements were performed on an LS spectrometer using a 100 mW Nd:YAG laser with a wavelength of $\lambda = 660$ nm. The sample temperature was kept at 293.1 ± 0.1 K via a thermostat-cooled decalin bath, and the temperature was measured by the goniometer built-in sensor. Cylindrical quartz cuvettes ($d = 10$ mm) were flushed with compressed air. Samples were prepared at a concentration of $c = 0.06$ g L^{-1} and purified three times from dust by passing the sample solution through a PTFE filter with a pore size of 5 µm directly into the dust-free cuvettes. To minimize laser after-pulsing artifacts, correlation functions were obtained using the Pseudo-Cross Correlation technique. Correlation functions were obtained at $\theta = 90°$ with an acquisition time of 60 s. All measurements were performed in triplicates. The recorded correlation functions were analyzed by applying the Cumulant and CONTIN methods using the LSI software package (v. 8.2.0.1). Size exclusion chromatography was used to obtain the number average molecular weight (M_n) and dispersity ($Đ$). For that, polymers were dissolved in tetrahydrofuran (THF) at a concentration of 1.5 g L^{-1}. The solution was filtered through a PTFE syringe filter (pore diameter of 0.2 µm) prior to being measured on a 1260 Infinity Instrument (PSS/Agilent, Mainz). The device was equipped with an isocratic pump, SDV PSS columns with porosities ranging from 10^2 to 10^6 Å, a differential refractometer, and a UV–Vis multiwavelength detector. For calibration, PS standards were used (PSS/Agilent, Mainz) with narrow size distributions and molecular weights ranging from 1000 to 1,000,000 g mol^{-1}.

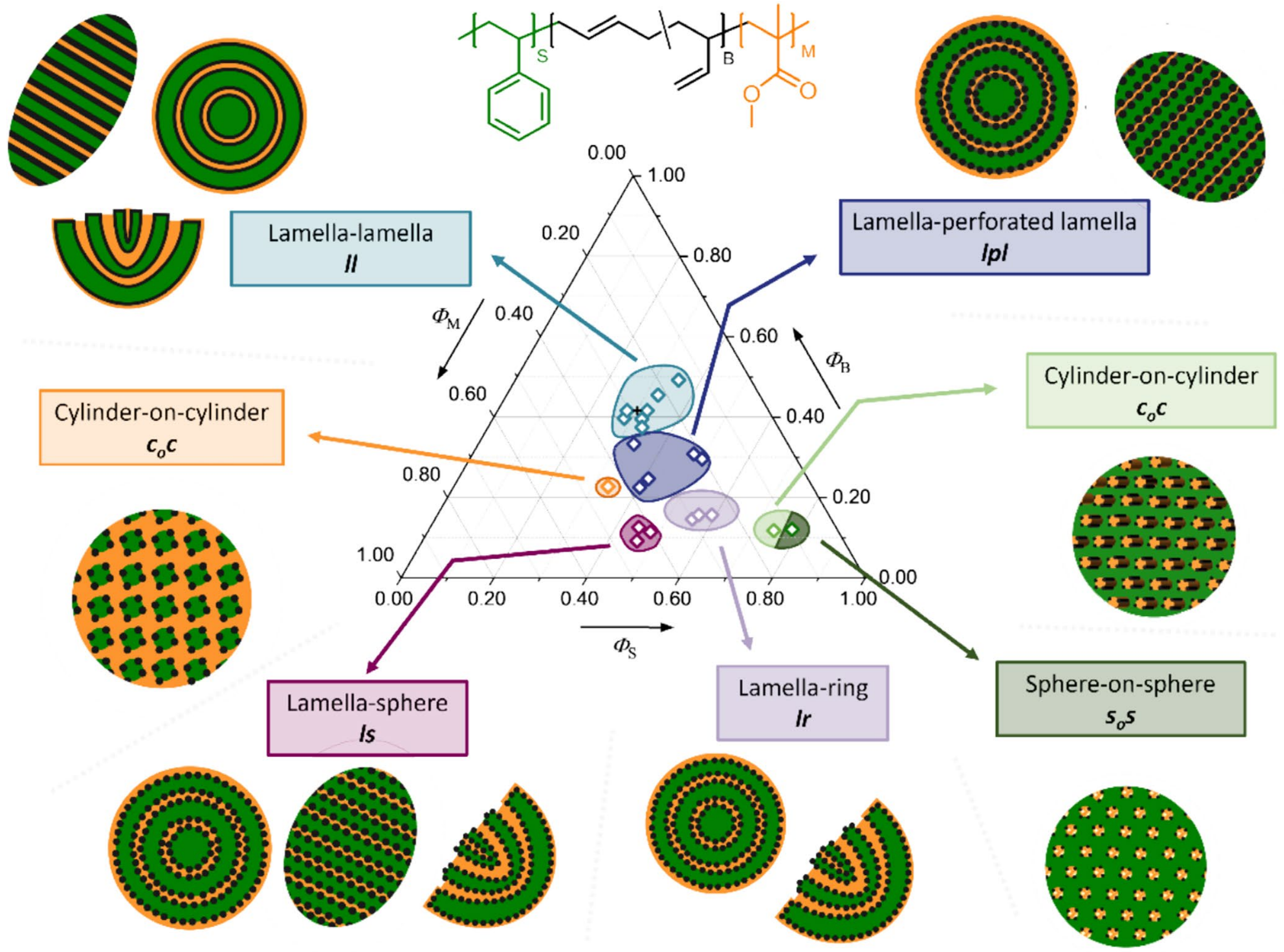

FIGURE 1 | Ternary microphase diagram of SBM in spherical confinement. Regions with different morphologies are indicated by different colors.

3 | Results and Discussion

3.1 | Ternary Microphase Diagram

All MPs were prepared following the same emulsification process (Figure S1). At first, SBM was dissolved in chloroform ($CHCl_3$) at a concentration of $c_{SBM} = 10\,g\,L^{-1}$, which is a good solvent for all blocks and immiscible with water [30, 37, 53]. Pressurized Argon was used to push the polymer solution through an SPG membrane with a pore diameter of $d_{pore} = 600\,nm$ into an aqueous SDS solution ($5\,g\,L^{-1}$) while stirring. Solid MPs were received after $CHCl_3$ evaporation and analyzed for their size distribution, shape, and inner structure. Following this procedure, we prepared MPs from a total of 22 SBMs with different block compositions and overall molecular weight. Size distributions of all MP samples were analyzed with DLS, which typically resulted in an average hydrodynamic diameter of the MPs of $d_h \approx 580$–$660\,nm$ (Figure S2). This diameter fits very well to the expected dimensions considering the 600 nm pore diameter and the used polymer concentration [39, 43]. The SPG membrane is a reliable method to produce MPs with rather narrow size dispersity, as confirmed by the low $Đ < 0.1$ in DLS as well as homogeneous sizes in SEM overview images (Figure S3).

Overall, we identified MPs with six different morphologies that we mapped into a ternary microphase diagram as summarized in Figure 1. Among the morphologies, we found lamella-lamella (*ll*), lamella-perforated lamella (*lpl*), lamella-ring (*lr*), lamella-sphere (*ls*), as well as sphere-on-sphere (s_os) and cylinder-on-cylinder (c_oc) in different matrices. These morphologies will be discussed in more detail in the individual sections below.

Evaporation is an inherently non-equilibrium process, where the outcome may depend on the specific processing pathway (Figure 2). To characterize the drying process, we introduce the dimensionless Péclet number (*Pe*), which describes the ratio between advective and diffusive motion of the confined solutes. We define the Péclet number as $Pe \equiv R_0^2/(D_0 t_{evap})$, where R_0 is the initial droplet radius, D_0 is the bulk diffusion coefficient of the terpolymers at the initial polymer concentration, and t_{evap} is the characteristic evaporation time. The typical parameters in our experiments are $R_0 \approx 2\,\mu m$, $D_0 \approx 90\,\mu m^2/s$, and $t_{evap} \sim 72\,h$, which leads to $Pe \sim 10^{-7} \ll 1$. Thus, the terpolymers should have sufficient time to relax into their preferred microphase before the solvent is fully evaporated from the droplet. We complement our experiments with coarse-grained molecular simulations of the respective SBM block compositions (see Supporting Information for model details). Each chain consists

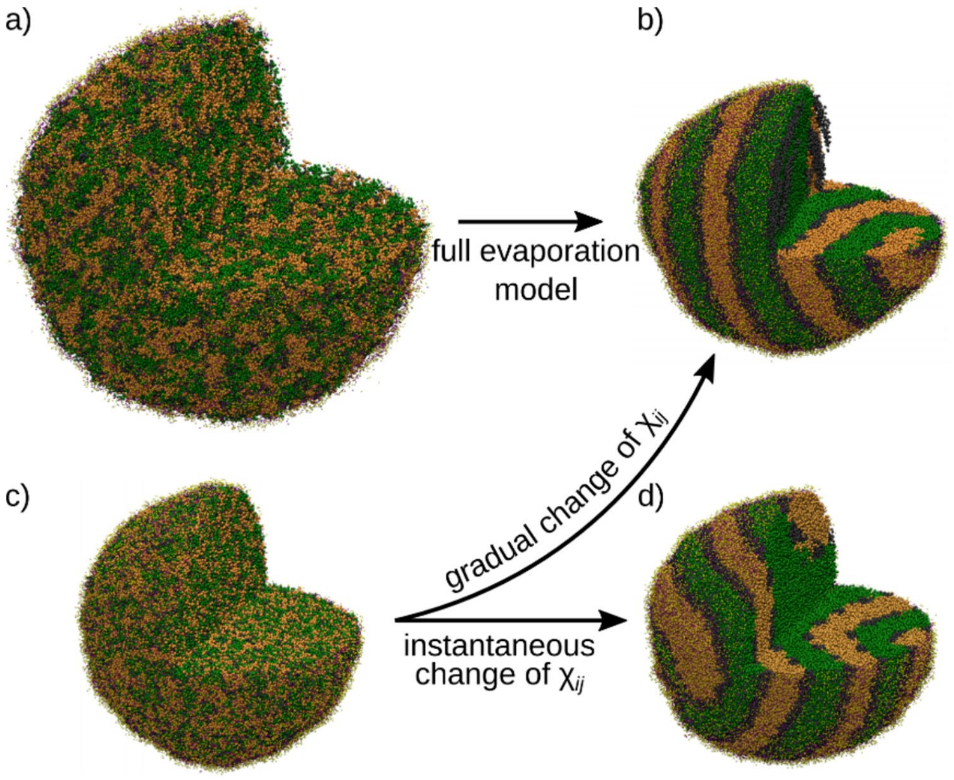

FIGURE 2 | Simulation snapshots showing truncated views of the (a, c) initial emulsion droplet and (b, d) final microparticle for $S_{45}B_{13}M_{42}$ from the two evaporation protocols. For clarity, chloroform and water particles have been removed from (a, b), and only every other surfactant molecule is drawn in panels (a–d).

of 39–123 beads, depending on the target SBM terpolymer, so that each bead represents 18–32 monomers, depending on its type. However, even for such a coarse polymer model, it is computationally impossible to achieve the experimental droplet sizes and evaporation times due to the large number of required particles and integration steps. Therefore, we scaled down the simulated droplets to $R_0 \approx 81\,\text{nm}$ and reduced the characteristic evaporation time to $t_{\text{evap}} \approx 110\,\mu\text{s}$, leading to $Pe \approx 0.6$ in our simulations. Thus, the simulations should also take place in the diffusion-dominated regime. To study the importance of the model details, we used two evaporation protocols to simulate the confinement assembly of the SBM terpolymers (Figure S10). In our first model, we model the $CHCl_3$ and water molecules as separate species and drive evaporation by periodically converting select $CHCl_3$ beads inside an evaporation zone to water beads. In the second model, we group the $CHCl_3$ and water molecules into the same bead and mimic solvent evaporation by gradually changing the interaction parameters over time. Although both techniques are conceptually different, they both ultimately led to the same MP morphology when the droplets were dried slowly (Figure 2), which supports our hypothesis that microphase separation in our setup occurs under quasi-equilibrium conditions.

To test the effect of evaporation rate on the self-assembly behavior, we performed additional simulations for $S_{45}B_{13}M_{42}$, where the interaction parameters were changed abruptly, that is $t_{\text{evap}} = 0$. In contrast, such a sudden change in effective solvent quality had a large impact on the final MP shape and internal microphase morphology, as the MPs did not have sufficient time to change from their initially spherical shape into an ellipsoid before the terpolymers microphase-separated (Figure 2d). These results suggest that the exact implementation of the evaporation procedure does not play an essential role in reaching the final MP shape and microphase morphology, if the systems are in the diffusion-dominated drying regime $Pe \lesssim 1$. However, this equivalency between the different protocols might not hold anymore in the evaporation-dominated regime $Pe \gtrsim 1$, where self-assembly occurs far from equilibrium. Since we are primarily interested in the self-assembly behavior in the diffusion-dominated regime, we performed the majority of simulations using the simplified evaporation procedure to expedite the simulations.

3.2 | The Lamella-Lamella Morphology

We start our discussion with SBMs that exhibit similar volumes for all three blocks, $\Phi_S = 0.28–0.35$, $\Phi_M = 0.16–0.32$, and $\Phi_B = 0.37–0.49$. Within this range, the eight compositions $S_{30}B_{42}M_{28}^{68}$, $S_{33}B_{37}M_{30}^{113}$, $S_{32}B_{40}M_{28}^{125}$, $S_{32}B_{41}M_{27}^{137}$, $S_{28}B_{40}M_{32}^{144}$, $S_{35}B_{49}M_{22}^{216}$, $S_{33}B_{45}M_{22}^{231}$, $S_{30}B_{42}M_{28}^{244}$ all resulted in the *ll*-morphology (Figure 3, Figure S5), and can thus be mapped into the middle of the microphase diagram (cyan region in Figure 1). The *ll*-morphology is observed more frequently in confinement assembly of BCPs because the range of suitable volume fractions tends to be large, for example $\Phi_A = 0.3–0.7$ for AB diblock copolymers. Although these eight SBMs form the *ll*-morphology, there are noticeable effects on the structure that originate from the overall SBM molecular weight M_n. For instance, we find an increase in lamella thickness with increasing

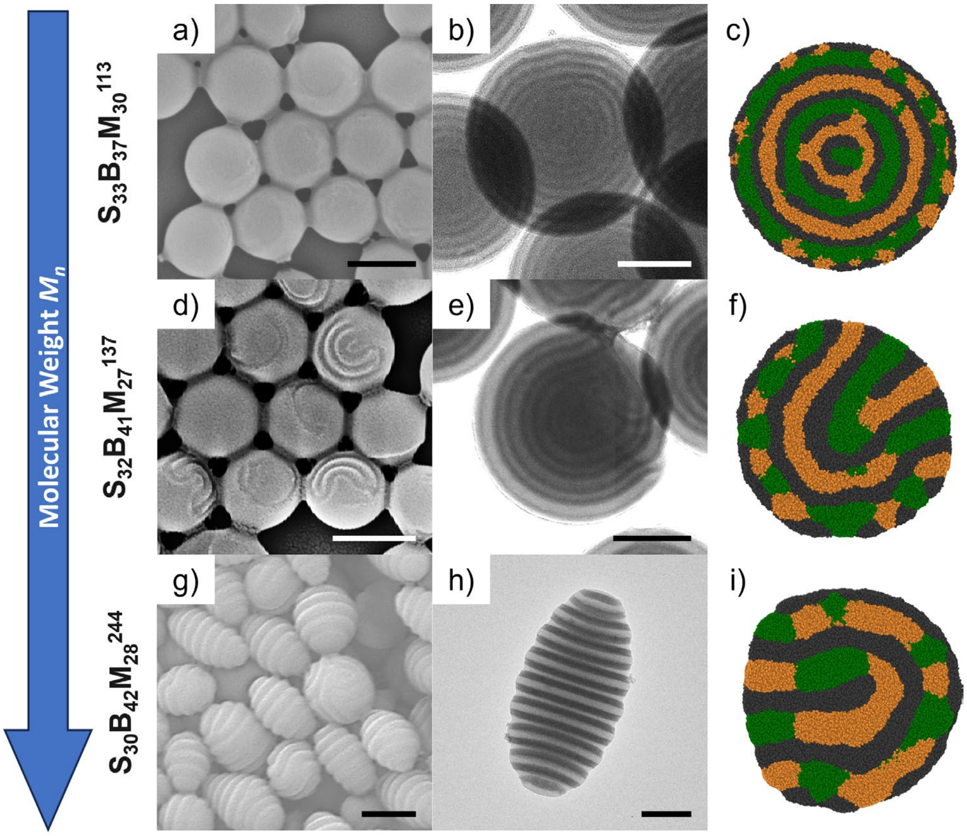

FIGURE 3 | MPs with *ll*-morphologies. (a–c) MPs of $S_{33}B_{37}M_{30}^{113}$ with spherical shape, (d–f) MPs of $S_{32}B_{41}M_{27}^{137}$ with tulip-bulb shape, and (g–i) MPs of $S_{30}B_{42}M_{28}^{244}$ with prolate ellipsoidal shape. (a, d, g) SEM, (b, e, h) TEM, and (c, f, i) simulation snapshots. Scale bars are 500 nm in SEM and 200 nm in TEM images.

M_n for all three lamellae (Figure 3), that is PS from 18 to 32 nm, PB from 17 to 32 nm, and PMMA from 16 to 20 nm (Figure S4). This trend is not surprising as blocks with larger M_n likewise require more volume and therefore lamellae increase in thickness. Similar observations have been reported before also for AB diblock copolymers [27]. That PMMA shows the smallest increase in lamella thickness can be attributed to a measurement artifact, where *e*-beam degradation caused shrinkage of the PMMA lamella during TEM measurements.

Interestingly, we find a change of lamella orientation with increasing M_n from concentric ($M_n = 68–125\,\text{kg mol}^{-1}$) to a mixture of concentric/tulip-bulb ($M_n = 137–216\,\text{kg mol}^{-1}$), and finally, axially stacked ($M_n > 231\,\text{kg mol}^{-1}$). Figure 3 compares three selected SBMs with similar composition ($\Phi_S/\Phi_M = 1.08–1.19$, $\Phi_B \approx 0.40$) but different M_n of 113, 137, and 244 kg mol^{-1}. At the lowest M_n, the lamellae of $S_{33}B_{37}M_{30}^{113}$ are arranged in a concentric manner leading to spherical MPs with a smooth surface (Figure 3a,b). In TEM, PMMA is barely visible as the outermost bright shell surrounding the darker Os-stained PB lamella. PMMA typically forms the outermost shell in such experiments because it is the most polar block and preferentially locates at the surfactant/water interface [37]. In the DPD simulations with the same block composition, we also find spherical MPs with concentric lamellae for low M_n, but perforated PB forms the outermost lamella (black in Figure 3c). This discrepancy might be explained by our assumption that PB preferably interacts with the hydrophobic tail of SDS (see Supporting Information); during drying, the interface is not a single molecular layer but rather a region of certain thickness that may display concentration profiles of $CHCl_3$, water, and SDS involving also preferential interactions with the polymer blocks. Water and SDS together are more polar than SDS alone, which could lead to the observed preference toward the more polar ester groups of PMMA instead of the modeled preference toward PB.

By increasing M_n to 137 kg mol^{-1} (Figure 3d–f), $S_{32}B_{41}M_{27}^{137}$ forms MPs with a tulip-bulb shape consisting of two hemispheres, where the bottom part corresponds to hemispheric concentric lamellae and the top part to axially stacked lamellae. In SEM, this kind of structural organization can be identified by both smooth and riffled surface features of the MPs (Figure 3d). This is further corroborated by TEM, where the hemispheric lamellae are clearly visible (Figure 3e). As M_n is roughly doubled in the DPD simulations while keeping the same block composition, the lamellae thickness increases as discussed above, but also MPs are not perfectly concentric anymore and show the onset of the tulip-bulb shape.

Upon further increase of M_n to 244 kg mol^{-1}, the transition continues and $S_{30}B_{42}M_{28}^{244}$ solely results in MPs with a pupa-like shape where all blocks form flat, axially stacked lamellae (Figure 3g,h). Lamella thickness increases in simulations as well, yet the MPs do not fully transform to a pupa-like shape, but instead we find a complete transition to the tulip-bulb shape. The differences between the experiments and simulations likely originate from finite-size effects, since the simulated MPs are roughly two times smaller in diameter compared to their experimental counterparts and thus contain fewer domains.

Overall, we attribute the transition from concentric lamellae to axially stacked lamellae to the preferential planar chain packing at the lamella interface and an increasing contribution of anisotropy to the MP shape. With increasing M_{n} and volume requirement of each block, bending of the lamella becomes progressively restricted due to entropically unfavorable chain compression (toward the MP center) and chain splay (toward the MP periphery). Therefore, it is reasonable that longer chains prefer planar chain packing in axially stacked lamellae instead of curved concentric lamellae. The extreme example of preferential planar packing would be 1D bottlebrush BCPs, as demonstrated in confinement assembly before [54]. Since the enthalpic interaction of the surfactant with each of the blocks appears to be of comparable magnitude (SDS does only show a minor preference for PMMA), the gain in energy through favorable interactions is not sufficient to force chains into bent lamellae [37].

3.3 | The Lamella-Perforated Lamella Morphology

Next, we discuss $S_{34}B_{33}M_{33}{}^{85}$, $S_{41}B_{23}M_{37}{}^{91}$, $S_{42}B_{25}M_{34}{}^{143}$, $S_{48}B_{28}M_{24}{}^{158}$, and $S_{50}B_{30}M_{20}{}^{159}$ ($\Phi_{\mathrm{PB}} = 0.23–0.33$, dark blue region in Figure 1). For these SBMs, we find perforated lamellae of PB sandwiched between lamellae of PS and PMMA, as for instance exemplified on $S_{41}B_{23}M_{37}{}^{91}$ in Figure 4 (see also Figure S5).

In SEM, the MPs show a smooth surface (Figure 4a) due to a concentric lamella arrangement of the blocks as confirmed also in TEM (Figure 4b). This morphology is expected because of a low M_{n} of 91 kg mol^{-1} and the almost equal-sized end blocks ($\Phi_{\mathrm{PS}}/\Phi_{\mathrm{PMMA}} = 1.11$). Again, PMMA forms the outermost shell, which is followed by PB and then PS. Owing to the perforation, it appears as if the PB simultaneously displays cylindrical and lamellar features, visible as dots and continuous stripes, respectively. These features can be seen more clearly in the corresponding cross-section TEM images (Figure 4c) and are corroborated by our simulations that likewise show a discontinuous PB domain appearing as perforated lamellae (Figure 4d). Unlike seen for the filled lamellae in Figure 3c,f,i, here the PB blocks appear as irregularly disrupted lines. We observed this morphology already before when we blended $S_{42}B_{25}M_{34}{}^{143}$ with low M_n PB in different ratios [53]. There, we observed that with increasing Φ_{PB}, the gaps between the perforated PB domains could be progressively filled to yield continuous PB-lamellae. This transition occurred between $\Phi_{\mathrm{PB}} = 0.36–0.40$, which is in the same range as the herein discussed example. Within our SBM library (Table 1, Figure S6), we find perforated lamellae up to $\Phi_{\mathrm{PB}} = 0.33$ ($S_{34}B_{33}M_{33}{}^{85}$) and complete PB-lamellae starting at $\Phi_{\mathrm{PB}} = 0.37$ ($S_{33}B_{37}M_{30}{}^{113}$). Comparing these values with the ones found via blending, it seems very likely that the critical transition threshold of Φ_{PB} for forming perforated instead of filled lamellae (and *vice versa*) is $\Phi_{\mathrm{PB},ll\leftrightarrow lpl} \approx 0.36–0.37$ [44].

3.4 | The Lamella-Ring and Lamella-Sphere Morphology

Next, we discuss $S_{55}B_{15}M_{30}{}^{127}$ and $S_{45}B_{9}M_{46}{}^{172}$ (Figure 5), which have roughly symmetric volumes of the end blocks and relatively small PB blocks of $\Phi_{\mathrm{PB}} = 0.15$ and $\Phi_{\mathrm{PB}} = 0.09$, respectively (lavender and purple region in Figure 1).

Starting with $S_{55}B_{15}M_{30}{}^{127}$, MPs exhibit a tulip-bulb shape (Figure 5a) with clearly visible lamellae of PS and PMMA. At $\Phi_{\mathrm{PB}} = 0.15$, PB forms cylinders between the lamellae that are less obvious in TEM but can be identified by their 1D anisotropy, leading to stripes or striations in TEM and cross-sections when viewed along the cylinder axis (Figure 5b,c). We observed this lamella-cylinder morphology before [32] and could show with ET that the cylinders are arranged in the form of concentric rings caused by the imposed curved confinement. We thus termed this structure lamella-ring (*lr*) morphology. Previously, we found this morphology for SBM only in MPs with a pupa-like shape (e.g., $S_{40}B_{22}M_{38}{}^{143}$), while polystyrene-*b*-poly(4-vinylpyridine)-*b*-poly(*tert*-butyl methacrylate) (SVT) with a composition of $S_{37}V_{12}T_{54}$ exclusively formed MPs with a tulip-bulb shape [55]. The MPs observed in the DPD simulations for a coarse-grained analogue of $S_{55}B_{15}M_{30}{}^{127}$ display a very similar morphology as in the experiments (Figure 5d), that is we obtain a tulip-bulb MP, where PB cylinders (black) are sandwiched between PS/PMMA lamellae (green and orange, respectively).

Moving on to $S_{45}B_{9}M_{46}{}^{172}$, we find pupa-like MPs (Figure 5e) probably as a result of the high M_{n} of 172 kg mol^{-1}, whereas

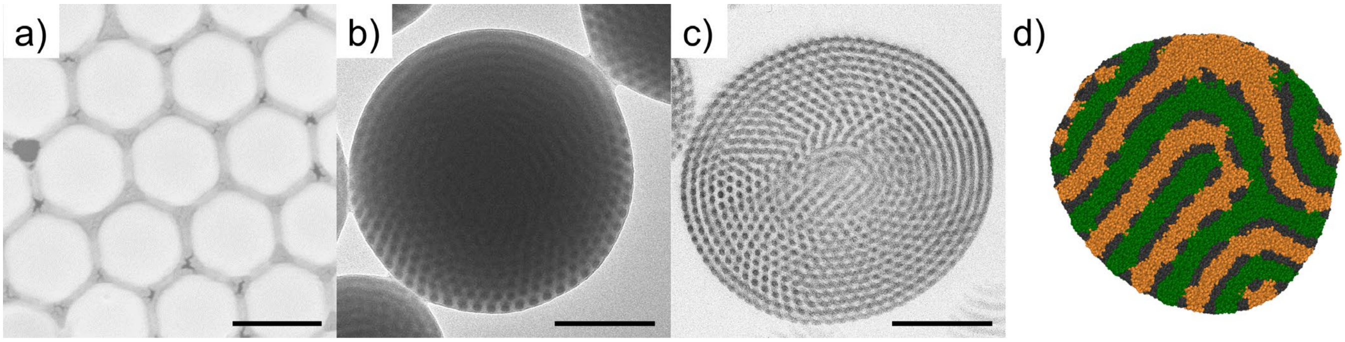

FIGURE 4 | MPs with *lpl* morphology. (a) SEM, (b) TEM, (c) TEM cross-section, and (d) simulation snapshot of $S_{41}B_{23}M_{37}{}^{91}$. Scale bars are 500 nm in SEM and 200 nm in TEM.

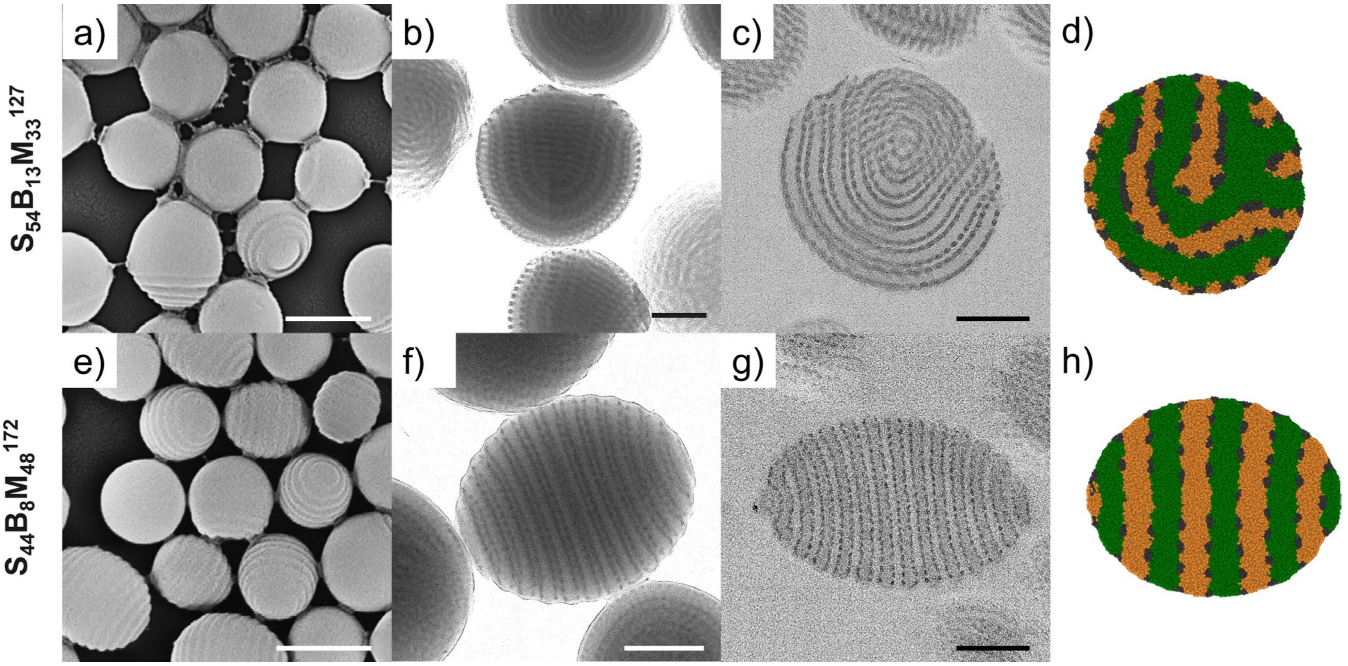

FIGURE 5 | MPs with *lr* and *ls* morphology. (a–d) MPs of $S_{55}B_{15}M_{30}{}^{127}$ with tulip-bulb shape and *lr*-morphology, that is PS/PMMA lamellae and PB rings. (e–h) MPs of $S_{46}B_{9}M_{45}{}^{172}$ with pupa-like shape and *ls*-morphology, that is axially stacked PS/PMMA lamellae and PB spheres. (a, e) SEM images of the MPs, (b, f) TEM images, (c, g) TEM cross-sections of MPs and (d, h) simulation snapshots of the respective morphology. PB appears darkest in TEM due to staining with OsO_4 (PS gray, PMMA brightest). Scale bars are 500 nm for SEM images and 200 nm for TEM images.

PS and PMMA blocks form axially stacked lamellae with PB spheres at their interface. Although the PB spheres are difficult to distinguish from PB cylinders in TEM projections (or cross-sections), they are isotropic and therefore do not display the typical striations as described above (Figure 5f,g). In the simulations, we also find lamellar domains for PS and PMMA, but PB still formed cylinders despite its relatively small volume fraction. We suspect that this behavior is linked to the χ parameters used for the simulations. Although the given set (Table S1) yields precise results when applied to compositions with *ll*-, *lpl*-, or *lr*-morphologies, it seems that χ_{SB} and χ_{BM} need to be increased for the correct prediction of PB spheres. To test this hypothesis, we performed simulations with significantly larger values of χ_{SB} and χ_{BM}, which indeed resulted in separated PB spheres (Figure S7). Similar to the discussion above, our SBM library (Table 1, Figure S8) allows for an estimation of critical Φ_{PB} values for the transitions perforated lamellae ↔ rings of $0.16 < \Phi_{PB,lpl\leftrightarrow lr} < 0.23$ and cylinders ↔ spheres $\Phi_{PB,lr\leftrightarrow ls} \approx 0.15$.

3.5 | Spheres-On-Spheres and Cylinders-On-Cylinders in PS Matrix

Next, we focus on SBMs in the PS-rich area of the microphase diagram (green regions in Figure 1), that is $S_{78}B_{12}M_{10}{}^{85}$ and $S_{74}B_{12}M_{14}{}^{89}$ with $\Phi_{PS} \geq 0.74$ and PB/PMMA together forming the minority microdomain (Figure 6). For $S_{78}B_{12}M_{10}{}^{85}$, we find spherical MPs with a smooth surface (Figure 6a). Within these MPs, we find PB spheres ($\Phi_{PB} = 0.12$) that are located on the surface of close-packed PMMA spheres ($\Phi_{PMMA} = 0.10$), embedded in a PS matrix (Figure 6b). We can exclude the formation of any anisotropic domains (such as cylinders), as we find the same pattern in TEM irrespective of viewing angle. Since PB and PMMA both form isotropic spheres, MPs are also exclusively spherical (we did not find any tulip-bulb or pupa-like MPs). The experimentally observed spherical microdomains embedded in a PS matrix are also in good agreement with the corresponding simulation snapshots shown in Figure 6c. There, only the PB microdomains are depicted (different colors for each microdomain for better distinction), which form (perforated) shells around PMMA spheres.

When the composition is changed to $S_{74}B_{12}M_{14}{}^{89}$, the increase in Φ_{PMMA} to 0.14 induces a morphological change from PMMA spheres to cylinders. The first indication for this transition can be taken from the SEM images, where the MPs are still spherical but now show a riffled surface (Figure 6d). In TEM, a hexagonal pattern can be recognized that we ascribe to hexagonally packed PMMA cylinders (Figure 6e), which are also supported by our DPD simulations (Figure 6f) and cross-section images (Figure S9). In the cross-sections, the hexagonal pattern becomes even more visible for those locations where the viewing direction is perpendicular to the cylinder cross-sections. Despite the unchanged volume of $\Phi_{PB} = 0.12$, the PB spheres seem to overlap on several occasions to form cylinders or a perforated shell surrounding the PMMA core. The simulation results depicted in Figure 6f corroborate this observation. In TEM imaging, we probably face a measurement artifact because shrinkage of the PMMA cylinders due to *e*-beam damage may considerably reduce the cylinder diameter, which in turn brings the PB spheres closer together up to a point where they appear to overlap into the observed morphology. An alternative explanation could be that the merging from PMMA spheres to cylinders comes at the cost of reduced cylinder diameter, which indeed brought PB spheres into closer contact.

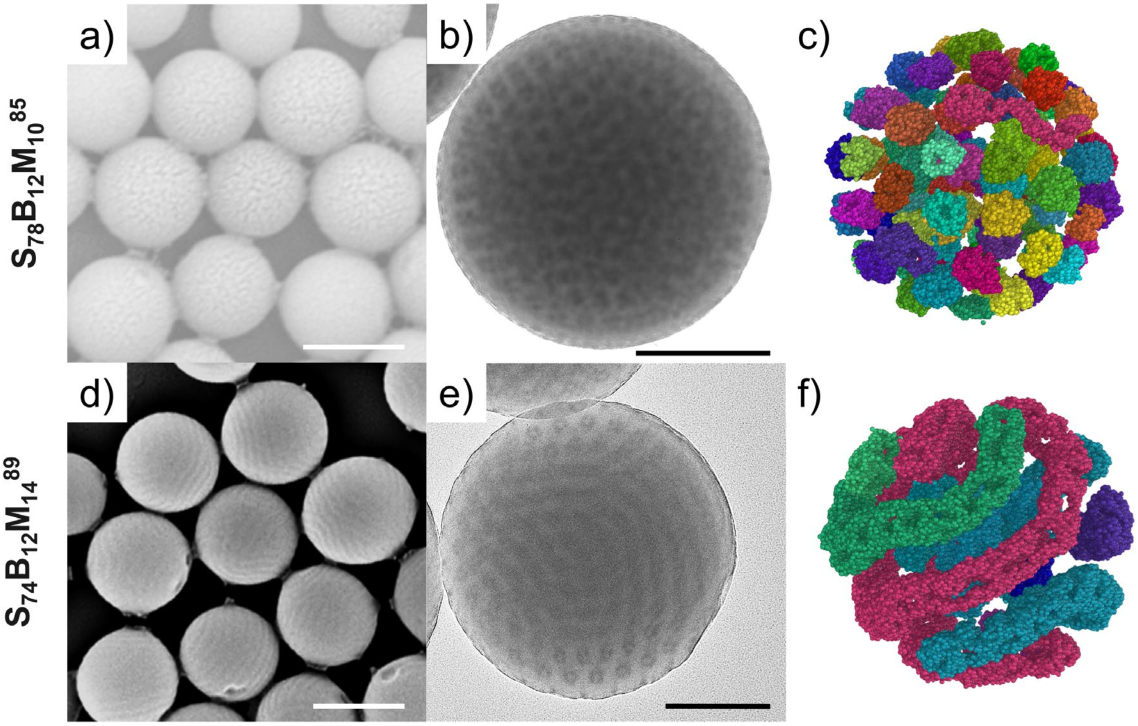

FIGURE 6 | MPs with $s_o s$ or $c_o c$-morphology in PS matrix. (a–c) MPs of $S_{78}B_{12}M_{10}{}^{85}$ with spherical shape and $s_o s$-morphology, that is PB spheres on PMMA spheres in a PS matrix, and (d–f) MPs of $S_{74}B_{12}M_{14}{}^{89}$ with spherical shape and $c_o c$-morphology, that is PB cylinders on hexagonally packed PMMA cylinders in a PS matrix. (a, d) SEM images of the MPs, (b, e) TEM images and (c, f) simulations of the respective morphology. Only PB is shown in the simulation snapshots, with each color representing an individual PB microdomain for better distinction. For TEM, PB was stained with OsO_4 rendering it darkest. Scale bars are 500 nm for SEM images and 200 nm for TEM images.

3.6 | Cylinders-On-Cylinders in PMMA Matrix

Lastly, we discuss the morphology of $S_{33}B_{23}M_{44}{}^{100}$ with the highest volume fraction of PMMA, $\Phi_{PMMA} = 0.44$ (orange area in Figure 1). Judging from the SEM images (Figure 7a), MPs of $S_{33}B_{23}M_{44}{}^{100}$ have an overall spherical shape while the MP surface displayed a surprisingly rich pattern that we assign to a cylinder-on-cylinder morphology. There, PS cylinders in dark gray are decorated with black PB cylinders and embedded in a bright PMMA matrix. Interestingly, this morphology is oriented both perpendicular and parallel to the MP surface instead of bending along the curved surface as often observed before for other cylinder morphologies in confinement. The MPs thus not only have a complex surface pattern, but also a complicated inner structure. Unfortunately, TEM imaging alone did not help to better understand the arrangement of the microdomains (Figure 7b), as the interpretation of the morphology was complicated by the many overlapping features and highly dependent on the particle orientation. The tilt series in Video S1 corroborates this observation. We thus prepared TEM cross-sections to reduce the number of overlapping features and utilized the tilt series to calculate a 3D reconstruction. From the cross-section, we could clearly assign PS and PB to cylinders because the longitudinal cylinder axes are visible as stripes and the cylinder bases as circular shapes (Figure 7c). The cylinder diameters measured $d_{cyl,PS} = 40$ nm and $d_{cyl,PB} = 19$ nm, respectively. From the combined results of cross-sectioning and reconstructions, the larger PS cylinders arrange in a cubic or monoclinic lattice. This lattice is less common than the typical hexagonal packing [52] and likely a result from the additional PB cylinders that themselves decorate the PS cylinder in a tetragonal manner. This PB arrangement can in turn be explained by the compromise of (i) minimization of interfacial area with PS cylinder, and (ii) the required volume of the PB microdomain (which does not allow six PB cylinders in hexagonal packing). The fact that the domain partially bends along and orients perpendicular to the curved interface might be related to the process of structure formation: During drying, the more hydrophobic PS block forms the cylinder microdomain prior to PMMA, which then is confined within the already highly concentrated spherical droplet. Due to its high bending rigidity, the PS cylinders may not close into rings entirely upon further droplet shrinking (unlike seen for the much softer PB). We tried to corroborate these hypotheses through DPD simulations, but there we observed completely different tulip-bulb-shaped MPs with PB on the outside and mixed PS and PMMA lamellae inside. This discrepancy between the experiments and simulations is quite surprising, given the generally good agreement for the other samples. One possible explanation for the mismatch could be the lack of glassiness in our DPD model, which allows the PS domains to fully relax.

4 | Conclusions

In the present study, we observed seven morphologies for 22 different SBM triblock terpolymers, which self-assembled in 3D confinement to yield solid MPs. Structural analysis was done using SEM, TEM, cross-sectioning, ET, and 3D

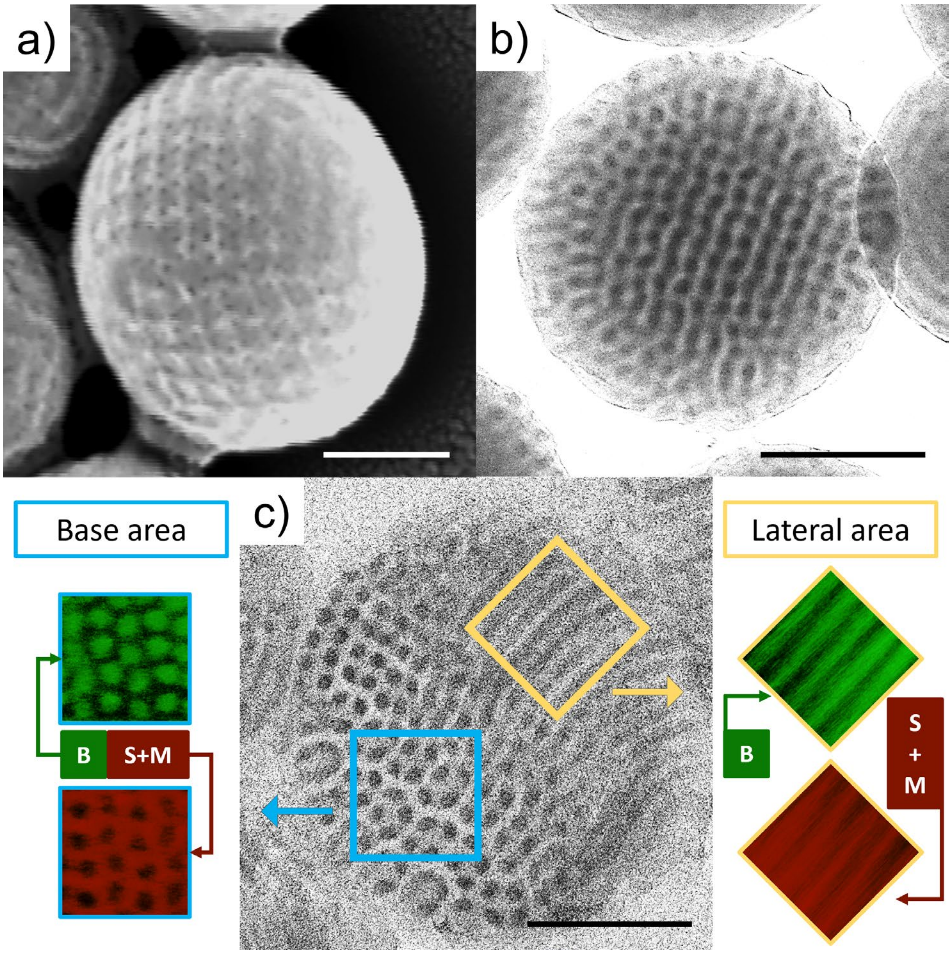

FIGURE 7 | The c_oc-morphology in PMMA matrix. (a) TEM image; PB is stained (OsO_4) and appears darkest. (b) SEM with PS (gray), PB (black), and PMMA (bright) distinguishable by contrast. (c) TEM of a cross section and 3D-reconstructions (in red and green). The cross section was additionally stained with RuO_4 and PS appears darker than PMMA. For the reconstruction the PB block is depicted in green and the PS and PMMA blocks in dark red. Scale bars are 200 nm.

reconstructions, and complemented by coarse-grained molecular simulations. Apart from more frequently observed lamellae-lamellae (*ll*), lamellae-ring (*lr*), lamellae-perforated lamellae (*lpl*) and lamellae-sphere (*ls*) morphologies, we also reported less common sphere-on-sphere (s_os) and cylinder-on-cylinder (c_oc) structures embedded in different matrices. For the lamella-inheriting structures, we proposed critical Φ_{PB}-values at which the morphologies are likely to transition between *ll* ↔ *lpl*, *lpl* ↔ *lr*, and *lr* ↔ *ls*. Derived from the *ll*-MPs, we also found the trend that with increasing M_n, the particles are more likely to form pupa-like ellipsoids with stacked lamellae (high M_n) instead of tulip-bulbs (medium M_n) or concentric spheres (low M_n); we explain the transition from curved to flat lamellae by the entropically unfavorable chain compression and chain splay occurring for the former, which become more pronounced with increasing chain length and toward the MP center. For shorter chains, this negative effect is compensated by preferential interfacial interactions that arise for a concentric arrangement. Concerning the s_os- and c_oc-MPs, especially the c_oc-morphology in a PMMA matrix is noteworthy due to the rather uncommon monoclinic- or cubically packed PS cylinders that stand perpendicular to the particle surface, which are reported for the first time in confinement. Our experiments and simulations are in good agreement for the large majority of samples, thus providing a helpful means for analyzing and cross-validating the emerging structures. Overall, the presented ternary microphase diagram delivers comprehensive information for the prediction of the inner structures of SBM triblock terpolymer-based MPs. We plan to broaden the scope of targetable structures further by employing homopolymer blending to increase the number of compositions and possibly accessible structures.

Acknowledgments

For access to SEM instruments the authors acknowledge the Münster Nanofabrication Facility (MNF). Part of this work was performed at the SoN—cryo-EM platform supported by the DFG, INST 211/1048-1 FUGG and the University of Münster. We also thank F. Hermann for his assistance in microtoming. This work was supported by the German Research Foundation (DFG project numbers 233630050, 445740352, 451785257 and 470113688). The authors gratefully acknowledge the computing time granted on the supercomputer Mogon (hpc.uni-mainz.de).

References

1. I. Vukovic, G. ten Brinke, and K. Loos, “Block Copolymer Template-Directed Synthesis of Well-Ordered Metallic Nanostructures,” *Polymer* 54, no. 11 (2013): 2591–2605, https://doi.org/10.1016/j.polymer.2013.03.013.

2. M. Radjabian and V. Abetz, “Advanced Porous Polymer Membranes From Self-Assembling Block Copolymers,” *Progress in Polymer Science* 102 (2020): 101219, https://doi.org/10.1016/j.progpolymsci.2020.101219.

3. A. Walther and A. H. E. Müller, “Janus Particles: Synthesis, Self-Assembly, Physical Properties, and Applications,” *Chemical Reviews* 113, no. 7 (2013): 5194–5261, https://doi.org/10.1021/cr300089t.

4. T. L. Nghiem, D. Coban, S. Tjaberings, and A. H. Gröschel, “Recent Advances in the Synthesis and Application of Polymer Compartments for Catalysis,” *Polymers* 12, no. 10 (2020): 2190, https://doi.org/10.3390/POLYM12102190.

5. H. Cabral, K. Miyata, K. Osada, and K. Kataoka, “Block Copolymer Micelles in Nanomedicine Applications,” *Chemical Reviews* 118, no. 14 (2018): 6844–6892, https://doi.org/10.1021/acs.chemrev.8b00199.

6. V. Abetz and A. Boschetti-de-Fierro, “Block Copolymers in the Condensed State,” in *Polymer Science: A Comprehensive Reference, 10 Volume Set*, vol. 7 (Elsevier, 2012), 3–44, https://doi.org/10.1016/B978-0-444-53,349-4.00192-8.

7. X. Qiang, R. Chakroun, N. Janoszka, and A. H. Gröschel, “Self-Assembly of Multiblock Copolymers,” *Israel Journal of Chemistry* 59, no. 10 (2019): 945–958, https://doi.org/10.1002/ijch.201900044.

8. Y. Mai and A. Eisenberg, “Self-Assembly of Block Copolymers,” *Chemical Society Reviews* 41, no. 18 (2012): 5969–5985, https://doi.org/10.1039/c2cs35115c.

9. A. H. Gröschel and A. H. E. Müller, “Self-Assembly Concepts for Multicompartment Nanostructures,” *Nanoscale* 7, no. 28 (2015): 11841–11876, https://doi.org/10.1039/c5nr02448j.

10. A.-C. Shi and B. Li, “Self-Assembly of Diblock Copolymers Under Confinement,” *Soft Matter* 9, no. 5 (2013): 1398–1413, https://doi.org/10.1039/C2SM27031E.

11. C. K. Wong, X. Qiang, A. H. E. Müller, and A. H. Gröschel, “Self-Assembly of Block Copolymers Into Internally Ordered Microparticles,” *Progress in Polymer Science* 102 (2020): 101211, https://doi.org/10.1016/j.progpolymsci.2020.101211.

12. K. H. Ku, J. M. Shin, H. Yun, G. R. Yi, S. G. Jang, and B. J. Kim, “Multidimensional Design of Anisotropic Polymer Particles From Solvent-Evaporative Emulsion,” *Advanced Functional Materials* 28, no. 42 (2018): 1, https://doi.org/10.1002/adfm.201802961.

13. M. Wang, X. Mao, J. Liu, et al., “A Versatile 3D-Confined Self-Assembly Strategy for Anisotropic and Ordered Mesoporous Carbon Microparticles,” *Advancement of Science* 9, no. 25 (2022): 2, https://doi.org/10.1002/advs.202202394.

14. Z. Wang, C. L. C. Chan, T. H. Zhao, R. M. Parker, and S. Vignolini, “Recent Advances in Block Copolymer Self-Assembly for the Fabrication of Photonic Films and Pigments,” *Advanced Optical Materials* 9, no. 21 (2021): 2100519, https://doi.org/10.1002/adom.202100519.

15. Y. Yang, H. Kim, J. Xu, et al., “Responsive Block Copolymer Photonic Microspheres,” *Advanced Materials* 30, no. 21 (2018): 1707344, https://doi.org/10.1002/adma.201707344.

16. Q. He, K. H. Ku, H. Vijayamohanan, B. J. Kim, and T. M. Swager, “Switchable Full-Color Reflective Photonic Ellipsoidal Particles,” *Journal of the American Chemical Society* 142, no. 23 (2020): 10424–10430, https://doi.org/10.1021/jacs.0c02398.

17. L. A. Connal, N. A. Lynd, M. J. Robb, et al., “Mesostructured Block Copolymer Nanoparticles: Versatile Templates for Hybrid Inorganic/Organic Nanostructures,” *Chemistry of Materials* 24, no. 21 (2012): 4036–4042, https://doi.org/10.1021/cm3011524.

18. K. H. Ku, M. P. Kim, K. Paek, et al., “Multicolor Emission of Hybrid Block Copolymer-Quantum Dot Microspheres by Controlled Spatial Isolation of Quantum Dots,” *Small* 9, no. 16 (2013): 2667–2672, https://doi.org/10.1002/smll.201202839.

19. K. H. Ku, J. M. Shin, D. Klinger, et al., “Particles With Tunable Porosity and Morphology by Controlling Interfacial Instability in Block Copolymer Emulsions,” *ACS Nano* 10, no. 5 (2016): 5243–5251, https://doi.org/10.1021/acsnano.6b00985.

20. R. Deng, S. Liu, J. Li, Y. Liao, J. Tao, and J. Zhu, “Mesoporous Block Copolymer Nanoparticles With Tailored Structures by Hydrogen-Bonding-Assisted Self-Assembly,” *Advanced Materials* 24, no. 14 (2012): 1889–1893, https://doi.org/10.1002/adma.201200102.

21. J. M. Shin, Y. Kim, K. H. Ku, et al., “Aspect Ratio-Controlled Synthesis of Uniform Colloidal Block Copolymer Ellipsoids From Evaporative Emulsions,” *Chemistry of Materials* 30, no. 18 (2018): 6277–6288, https://doi.org/10.1021/acs.chemmater.8b01821.

22. R. Deng, F. Liang, W. Li, et al., “Shaping Functional Nano-Objects by 3D Confined Supramolecular Assembly,” *Small* 9, no. 24 (2013): 4099–4103, https://doi.org/10.1002/smll.201300271.

23. K. H. Ku, Y. J. Lee, Y. Kim, and B. J. Kim, “Shape-Anisotropic Diblock Copolymer Particles From Evaporative Emulsions: Experiment and Theory,” *Macromolecules* 52, no. 3 (2019): 1150–1157, https://doi.org/10.1021/acs.macromol.8b02465.

24. L. Navarro, A. F. Thünemann, and D. Klinger, “Solvent Annealing of Striped Ellipsoidal Block Copolymer Particles: Reversible Control Over Lamellae Asymmetry, Aspect Ratio, and Particle Surface,” *ACS Macro Letters* 11, no. 3 (2022): 329–335, https://doi.org/10.1021/acsmacrolett.1c00665.

25. J. M. Shin, Y. Kim, H. Yun, G. R. Yi, and B. J. Kim, “Morphological Evolution of Block Copolymer Particles: Effect of Solvent Evaporation Rate on Particle Shape and Morphology,” *ACS Nano* 11, no. 2 (2017): 2133–2142, https://doi.org/10.1021/acsnano.6b08342.

26. S.-J. Jeon, G.-R. Yi, and S.-M. Yang, “Cooperative Assembly of Block Copolymers With Deformable Interfaces: Toward Nanostructured Particles,” *Advanced Materials* 20, no. 21 (2008): 4103–4108, https://doi.org/10.1002/adma.200801377.

27. D. Klinger, C. X. Wang, L. A. Connal, et al., “A Facile Synthesis of Dynamic, Shape-Changing Polymer Particles,” *Angewandte Chemie* 53, no. 27 (2014): 7018–7022, https://doi.org/10.1002/anie.201400183.

28. J. Lee, K. H. Ku, J. Kim, Y. J. Lee, S. G. Jang, and B. J. Kim, “Light-Responsive, Shape-Switchable Block Copolymer Particles,” *Journal of the American Chemical Society* 141, no. 38 (2019): 15348–15355, https://doi.org/10.1021/jacs.9b07755.

29. J. Xu, K. Wang, J. Li, H. Zhou, X. Xie, and J. Zhu, “ABC Triblock Copolymer Particles With Tunable Shape and Internal Structure Through 3D Confined Assembly,” *Macromolecules* 48, no. 8 (2015): 2628–2636, https://doi.org/10.1021/acs.macromol.5b00335.

30. J. Xu, Y. Yang, K. Wang, et al., “Additives Induced Structural Transformation of ABC Triblock Copolymer Particles,” *Langmuir* 31, no. 40 (2015): 10975–10982, https://doi.org/10.1021/acs.langmuir.5b02843.

31. N. Janoszka, S. Azhdari, C. Hils, D. Coban, H. Schmalz, and A. H. Gröschel, “Morphology and Degradation of Multicompartment Microparticles Based on Semi-Crystalline Polystyrene-Block-Polybutadiene-Block-Poly(L-Lactide) Triblock Terpolymers,” *Polymers* 13, no. 24 (2021): 4358, https://doi.org/10.3390/polym13244358.

32. A. Steinhaus, R. Chakroun, M. Mullner, T. L. Nghiem, M. Hildebrandt, and A. H. Groschel, “Confinement Assembly of ABC Triblock Terpolymers for the High-Yield Synthesis of Janus Nanorings,” *ACS Nano* 13, no. 6 (2019): 6269–6278, https://doi.org/10.1021/acsnano.8b09546.

33. X. Qiang, X. Dai, A. Steinhaus, and A. H. Gröschel, "Multicompartment Microparticles With Patchy Topography Through Solvent-Adsorption Annealing," *ACS Macro Letters* 8, no. 12 (2019): 1654–1659, https://doi.org/10.1021/acsmacrolett.9b00713.

34. X. Qiang, S. Franzka, G. Quintieri, X. Dai, C. K. Wong, and A. H. Gröschel, "Size-Controlled Formation of Polymer Janus Discs," *Angewandte Chemie International Edition* 60, no. 40 (2021): 21668–21672, https://doi.org/10.1002/anie.202105235.

35. P. Hiekkataipale, T. I. Löbling, M. Poutanen, et al., "Controlling the Shape of Janus Nanostructures Through Supramolecular Modification of ABC Terpolymer Bulk Morphologies," *Polymer* 107 (2016): 456–465, https://doi.org/10.1016/j.polymer.2016.05.076.

36. X. Qiang, A. Steinhaus, C. Chen, R. Chakroun, and A. H. Gröschel, "Template-Free Synthesis and Selective Filling of Janus Nanocups," *Angewandte Chemie, International Edition* 58, no. 21 (2019): 7122–7126, https://doi.org/10.1002/anie.201814014.

37. M. Trömer, E. M. Zirdehi, A. Nikoubashman, and A. H. Gröschel, "Effect of Surfactant Selectivity on Shape and Inner Morphology of Triblock Terpolymer Microparticles," *Macromolecular Rapid Communications* 44, no. 15 (2023): 2300123, https://doi.org/10.1002/marc.202300123.

38. S. Azhdari, Y. Post, M. Trömer, D. Coban, G. Quintieri, and A. H. Gröschel, "Janus Nanoplates, -Bowls, and -Cups: Controlling Size and Curvature via Terpolymer/Homopolymer Blending in 3D Confinement," *Nanoscale* 15, no. 36 (2023): 14896–14905, https://doi.org/10.1039/d3nr02902f.

39. M. Trömer, A. Nikoubashman, and A. H. Gröschel, "Multicompartment Microparticles of SBM Triblock Terpolymers: Morphological Transitions Through Homopolymer Blending," *Colloid & Polymer Science* 302, no. 12 (2024): 1957–1966, https://doi.org/10.1007/s00396-024-05320-4.

40. N. Yan, Y. Zhu, and W. Jiang, "Self-Assembly of ABC Triblock Copolymers Under 3D Soft Confinement: A Monte Carlo Study," *Soft Matter* 12, no. 3 (2016): 965–972, https://doi.org/10.1039/c5sm02079d.

41. J. Zhang, W. Kong, and H. Duan, "Soft Confinement-Induced Morphologies of the Blends of AB Diblock Copolymers and C Homopolymers," *Langmuir* 33, no. 12 (2017): 3123–3133, https://doi.org/10.1021/acs.langmuir.7b00181.

42. X. Liu, C. Zhou, H. Xia, Y. Zhou, and W. Jiang, "Dissipative Particle Dynamics Simulation on the Self-Assembly of Linear ABC Triblock Copolymers Under Rigid Spherical Confinements," *E-Polymers* 17, no. 4 (2017): 321–331, https://doi.org/10.1515/epoly-2016-0306.

43. A. Steinhaus, D. Srivastva, X. Qiang, S. Franzka, A. Nikoubashman, and A. H. Groschel, "Controlling Janus Nanodisc Topology Through ABC Triblock Terpolymer/Homopolymer Blending in 3D Confinement," *Macromolecules* 54, no. 3 (2021): 1224–1233, https://doi.org/10.1021/acs.macromol.0c02769.

44. T. Goldacker and V. Abetz, "A New Way to the "Knitting Pattern" via Blending of ABC Triblock Copolymers," *Macromolecular Rapid Communications* 20, no. 8 (1999): 415–418.

45. U. Breiner, U. Krappe, V. Abetz, and R. Stadler, "Cylindrical Morphologies in Asymmetric ABC Triblock Copolymers," *Macromolecular Chemistry and Physics* 198, no. 4 (1997): 1051–1083, https://doi.org/10.1002/macp.1997.021980411.

46. R. Stadler, C. Auschra, J. Beckmann, U. Krappe, I. Voigt-Martin, and L. Leibler, "Morphology and Thermodynamics of Symmetric Poly(A-Block-B-Block-C) Triblock Copolymers," *Macromolecules* 28, no. 9 (1995): 3080–3097, https://doi.org/10.1021/ma00113a010.

47. T. I. Löbling, P. Hiekkataipale, A. Hanisch, et al., "Bulk Morphologies of Polystyrene-Block-Polybutadiene-Block-Poly(Tert-Butyl Methacrylate) Triblock Terpolymers," *Polymer* 72 (2015): 479–489, https://doi.org/10.1016/j.polymer.2015.02.025.

48. X. Qiang, S. Franzka, X. Dai, and A. H. Gröschel, "Multicompartment Microparticles of SBT Triblock Terpolymers Through 3D Confinement Assembly," *Macromolecules* 53, no. 11 (2020): 4224–4233, https://doi.org/10.1021/acs.macromol.0c00806.

49. J. M. Shin, M. P. Kim, H. Yang, et al., "Monodipserse Nanostructured Spheres of Block Copolymers and Nanoparticles via Cross-Flow Membrane Emulsification," *Chemistry of Materials* 27, no. 18 (2015): 6314–6321, https://doi.org/10.1021/acs.chemmater.5b02020.

50. C. Auschra and R. Stadler, "Synthesis of Block Copolymers With Poly(Methyl Methacrylate): P(B-b-MMA), P(EB-b-MMA), P(S-b-B-b-MMA) and P(S-b-EB-b-MMA)," *Polymer Bulletin* 30, no. 3 (1993): 257–264, https://doi.org/10.1007/BF00343058.

51. J. R. Kremer, D. N. Mastronarde, and J. R. McIntosh, "Computer Visualization of Three-Dimensional Image Data Using IMOD," *Journal of Structural Biology* 116, no. 1 (1996): 71–76, https://doi.org/10.1006/jsbi.1996.0013.

52. E. F. Pettersen, T. D. Goddard, C. C. Huang, et al., "UCSF Chimera—A Visualization System for Exploratory Research and Analysis," *Journal of Computational Chemistry* 25, no. 13 (2004): 1605–1612, https://doi.org/10.1002/jcc.20084.

53. M. D. Abràmoff, P. J. Magalhães, and S. J. Ram, "Image Processing With ImageJ," *Biophotonics International* 11, no. 7 (2004): 36–41, https://doi.org/10.1201/9781420005615.ax4.

54. S. Andrea, T. Pelras, R. Chakroun, et al., "Self-Assembly of Diblock Molecular Polymer Brushes in the Spherical Confinement of Nanoemulsion Droplets," *Macromolecular Chemistry and Physics* 39, no. 19 (2018): 1800177, https://doi.org/10.1002/marc.201800177.

55. Q. Giada, M. Saccone, M. Spengler, et al., "Supramolecular Modification of ABC Triblock Terpolymers in Confinement Assembly," *Nanomaterials* 8, no. 12 (2018): 1029, https://doi.org/10.3390/nano8121029.

Supporting Information

Additional supporting information can be found online in the Supporting Information section.